applied sciences

MDPI

Article

A Differential Measurement System for Surface Topography based on a Modular Design

Fang Cheng [1,*], Jingwu Zou [1], Hang Su [1], Yin Wang [1] and Qing Yu [1]

College of Mechanical Engineering and Automation, Huaqiao University, Xiamen, 361021, China; zoujingwu96@163.com (J.Z.); 18351965378@163.com (H.S.); yin.wangyin@hqu.edu.cn (Y.W.); yuqing@hqu.edu.cn (Q.Y.)

* Correspondence: chf19chf19@hotmail.com and chengfang@hqu.edu.cn

Received: 15 January 2020; Accepted: 21 February 2020; Published: 24 February 2020

Abstract: In this paper, a novel design of a surface topography measurement system is proposed, to address the challenge of accurate measurement in a relatively large area. This system was able to achieve nanometer-scale accuracy in a measurement range of 100 mm x 100 mm. The high accuracy in a relatively large area was achieved by implementing two concepts: (1) A static coordinate system was configured to minimize the Abbe errors. (2) A differential measurement configuration was developed by setting up a confocal sensor and a film interferometry module to separate the motion error. In order to accommodate the differential measurement probes from both sides of the central stage and ensure the system rigidity with balanced supports, separate linear guides were introduced in this system. Therefore, the motion Degree of Freedom (DoF) was analyzed in order to address the challenge of an over-constrained mechanism due to multiple kinematic pairs. An optimal configuration and a quick assembly process were proposed accordingly. The experimental results presented in this paper showed that the proposed modular measurement system was able to achieve 10 nm accuracy in measuring the surface roughness and 100 nm accuracy in measuring the step height in the range of 100 mm x 100 mm. In summary, the novel concept of this study is the build of a high-accuracy system with conventional mechanical components.

Keywords: topography measurement; differential measurement system; modular design; confocal sensor; film interferometry; over-constrained mechanism.

1. Introduction

Surface topography measurement [1–3] is an important metrological tool for quality assessment in industries that include semiconductors [4,5], micro-electromechanical system (MEMS) [6], additive manufacturing [7], and aerospace [8]. A common challenge with developing surface metrology technologies is the achievement of multi-scale measurement capability, which means high accuracy over a large measurement area.

Optical approaches that are playing important roles in this area [9,10], such as confocal microscopy [11,12], coherence scanning interferometry [13], and focus variation [14], are able to meet nanometer accuracy, but the measurement range is within a few millimeters or even smaller. The data stitching technique is able to expand the measurement range, but it relies heavily on common features of the overlapping area from neighboring data sets [15]. If the overlapping area does not show distinct features, the stitching accuracy will rely heavily on the performance aspects of the motion system, such as the straightness and flatness [16].

Therefore, high-precision 2D/3D positioning [17] is a key technical enabler for multi-scale measurement systems. In reference [18], an optical probe was mounted on a Coordinate Measuring Machine (CMM). In references [19,20], Scanning Probe Microscopy (SPM) probes were equipped with high-precision positioning systems, to achieve a sub-nanometer resolution in a millimeter measurement area.

When integrating a high-accuracy probe with a motion system, there are two types of critical measurement errors that researchers have to consider. They are the motion error, introduced by the imperfect straightness of the guideway [21,22], and the Abbe error, introduced by the system design [23,24]. Motion errors can be minimized by using high-precision components as geometric references [25]. However, the accuracy loss of mechanical references is inevitable after heavy usage. The motion error can also be compensated by implementing differential measurement [26,27] or by introducing additional optical measurement systems [28,29]. The Abbe error can be minimized by employing a static coordinate system in which the position sensors track the central stage along the coordinate axis [30,31]. In reference [30], three laser interferometers that formed a static coordinate system were used to track the position of the central stage. In reference [31], the central stages were mechanically tracked by optical encoders. However, both concepts have their drawbacks. Optical tracking is very sensitive to environmental disturbances such as temperature and airflow. Mechanical tracking systems require a very complicated assembly and adjustment process due to the over-constrained mechanism. Furthermore, the geometric accuracy of the mechanical components will significantly affect the measurement accuracy.

In order to address the challenges discussed in the above paragraph, a modular system for surface topography measurement was developed using conventional components. The central stages were mechanically tracked by optical encoders with consideration of the cost and robustness [31]. An optimal system design was proposed in order to address the challenge of the over-constrained mechanism. A film interferometer was developed to compensate for the straightness error from the motion system.

The motivation and scope of the presented work can be illustrated by the graphic abstract shown in Figure 1.

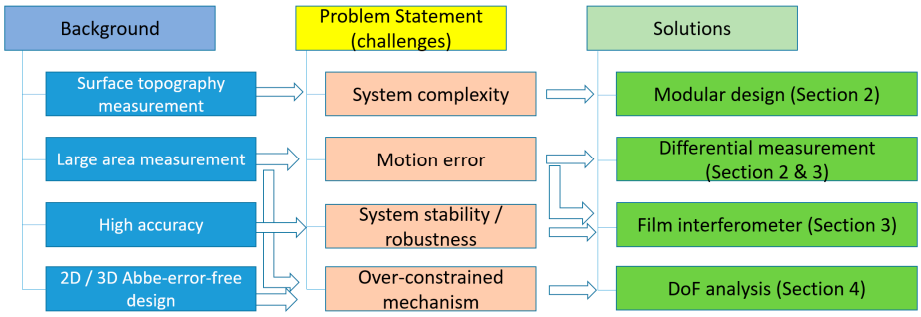

Figure 1. Graphic abstract.

2. Overall system design

The system configuration of the proposed design is shown in Figure 2. The overall dimension of the system is L 890 mm × W 820 mm × H 675 mm. The measurement range is 100 mm × 100 mm × 50 mm. Like the first prototype, this system was built of aluminum alloy. The central stage was supported by two sets of 2D sliders and driven by a pair of actuators (Zolix uKSA 100, Zolix Instruments CO.,LTD, Beijing, China). Each uKSA 100 is able to achieve a travel range of 100 mm, which determined the measurement range of the presented system.

A confocal sensor, Precitec CHRocodile SE (Precitec Group, Germany), was mounted on the main spindle to measure the height at each location of the test piece. This confocal sensor was able to achieve 3 nm resolution in a measurement range of 600 μm. An optical flat [32] (ϕ 300 mm × T 30 mm, K9 glass) was placed in the center of the stage as the geometric datum. A film interferometer was developed in order to configure a differential measurement system with the confocal sensor. During the lateral movement, the film interferometer was used to compensate for the straightness error by measuring the fluctuation of the optical plat from the bottom.

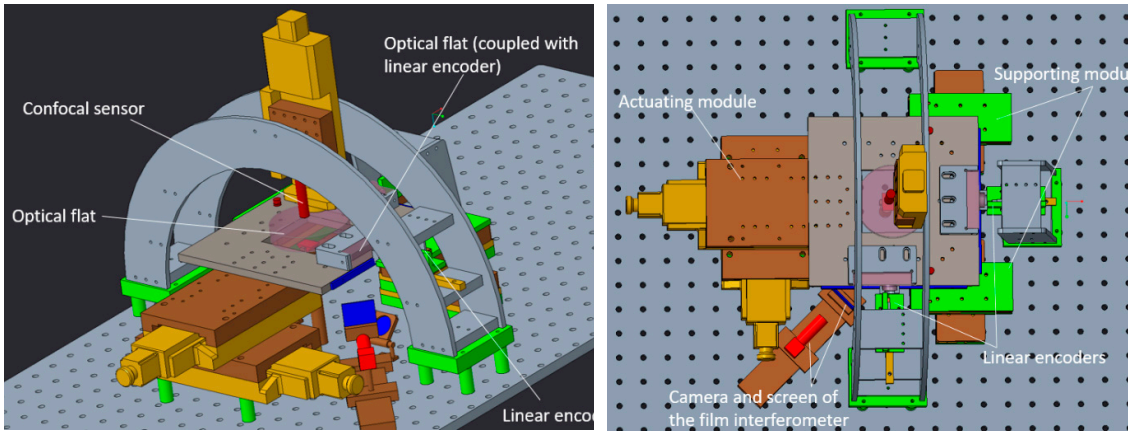

(**a**) Side view (**b**) Top view

Figure 2. System design: (**a**) Side view, (**b**) Top view.

The XY positions were measured by linear encoders, which were coupled with the central stage through contact kinematic pairs. Each contact kinematic pair consisted of two optical flats, which helped to minimize the coupling errors. The linear encoders only moved along the measurement axes. In the XY plane, therefore, a static coordinate system was formed by the linear encoders, and the system complied with the Abbe principle [23,24].

In this system, the position measurement accuracy relied on the datum features formed by the optical flats, instead of the mechanical translation components. All of the linear guides used in this system were within the ordinary accuracy range.

The geometric error factors for the height measurement are shown in Figure 3. The actual height of the measurement point could be expressed as:

$$h = h_1 - h_2 - h_3 - \left(\frac{T}{cos\theta} - T\right). \quad (1)$$

In Equation (1) h_1 is the height measured by the confocal sensor, h_2 represents the motion error caused by the linear guides, and h_3 is the height fluctuation due to the flatness error of the optical flat. T is the thickness of the optical flat and θ is its tilting angle during the movement.

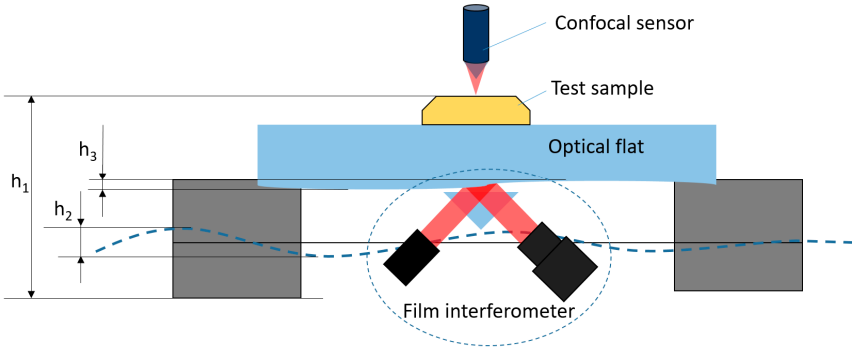

(**a**) Straightness and flatness

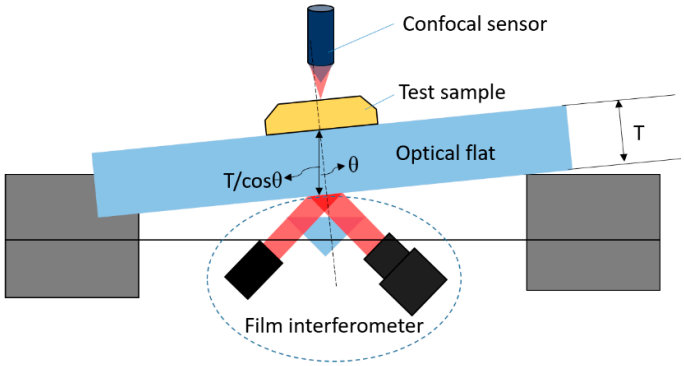

(**b**) Tilting angle

Figure 3. Geometric error factors: (**a**) Straightness and flatness, (**b**) Tilting angle.

In this system, the flatness of the optical flat was ±25 nm. The thickness of the optical flat was 30 mm. By assuming that the angular motion error was no greater than 20″, the maximum height measurement error $T(1-cos\theta)$ could be calculated to be 0.14 nm. Therefore, the values of h_3 and $T(1-cos\theta)$ were very insignificant and Equation (1) could be simplified as:

$$h = h_1 - h_2, \tag{2}$$

where h_2 was mainly contributed by the straightness error of the linear guide and it could be measured by the film interferometer.

Instead of an all-in-one structure, the concept of modular design was employed in the proposed system. As shown in Figure 2, the system was assembled with a few functional modules:

1) An actuating module, which consisted of two motorized stages.
2) Supporting modules, each of which consisted of pre-assembled 2D sliders
3) A differential height measurement module, which consisted of a confocal sensor and a film interferometer
4) A displacement measurement module, which consisted of an optical gratings couple with the central stage through optical flats.
5) A datum module, which consisted of three optical flats.

Since these functional modules were all commercially available components, no special design or assembly processes were needed in the proposed system.

3. Motion error compensation based on a film interferometer

As described in the section above, the motion error caused by the linear guide represented by h_2 was measured by an in-house developed film interferometer. The principle is shown in Figure 4.

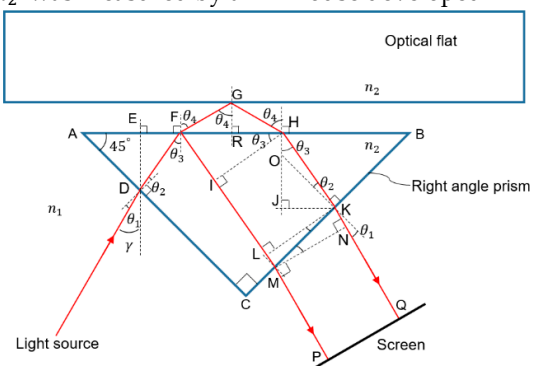

(**a**) Principle

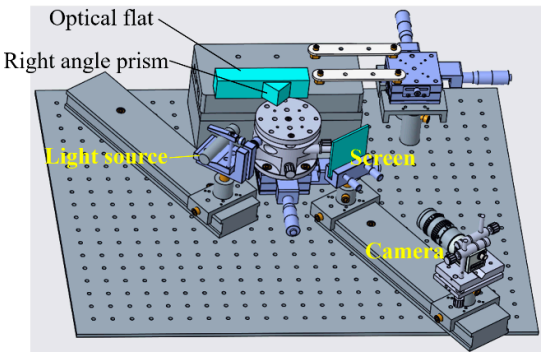

(**b**) Off-line testing setup

Figure 4. Principle of the film interferometer: (**a**) Principle, (**b**) Off-line testing setup.

The key specifications of the components used in this system are listed in Table 1.

Table 1. Component specifications in the film interferometer.

Components	Specifications
Camera	Basler acA2000-165um, frame rate 165 fps, resolution 2048×1088 (2 MP)
Lens	Moritex ML - MC50HR, 0.8×, focal length 50mm
Right-angle prism	25.4 mm × 25.4 mm × 25.4 mm, K9 glass, refractive index 1.5163

As shown in Figure 4a, the film interferometer included two optical components, the optical flat and the right-angle prism. The optical flat moved with the stage and the right-angle prism was stationary. The two optical surfaces formed an air gap between themselves with a gradually changing thickness. The incident laser beam was split and reflected by the two optical surfaces. When the angle of the air gap was very small, the reflected laser beams propagated along the same path and generated an interferogram that was detected by the camera. By analyzing the phase shift of the interferogram, the distance variation between the optical flat and the right-angle prism could be measured. This distance variation represented the motion error caused by the imperfect straightness of the linear guide.

The root cause of the interferogram was the optical path difference of the reflected beams from the two optical surfaces. As shown in Figure 4a, the optical path difference D could be expressed as:

$$\mathrm{D} = \mathrm{n}_1(\mathrm{FG} + \mathrm{GH} + \mathrm{KN}) + n_2 \cdot \mathrm{HK} - \mathrm{n}_2(\mathrm{FI} + \mathrm{IL} + \mathrm{LM}), \tag{3}$$

where n_1 and n_2 are the relative refractive indexes of the air and glass, respectively, and $\lambda/2$ represents the half-wave rectification. Based on geometrically analyzing the optical path, it could be concluded that:

1) Since the angle of the air gap was very small, FG was approximately equal to GH:

$$FG = GH. \tag{4}$$

2) Since HK and IL could be seen as the same light beam in the same medium, HK was equal to IL:

$$HK = IL. \tag{5}$$

3) Since LM and KN could be seen as the same light beam in different media, they had the same length of the optical path:

$$n_2 \cdot LM = n_1 \cdot KN \tag{6}$$

It should be highlighted that Equation (4)–(6) were approximately true because the optical flat was not ideally parallel with the bottom of the right-angle prism. When the angle between the two reflective surfaces was very small, the optical path differences $FG - GH$, $HK - IL$, and $n_2 \cdot LM - n_1 \cdot KN$ could be considered as a higher-order infinitesimal of the angle.

With Equation (5)–(7) substituted into Equation (4), the optical path difference could be expressed as:

$$\mathrm{D} = 2\mathrm{n}_1 \cdot FG - n_2 \cdot FI. \tag{7}$$

By assuming that the current distance between the two optical surfaces was GR=d, D could be modified as:

$$\mathrm{D} = \frac{2\mathrm{n}_1 d}{\cos\theta_4} - \frac{2n_2 d \sin\theta_3}{\tan\theta_4}. \tag{8}$$

Based on Shell's law,

$$\begin{cases} n_2 sin\theta_3 = n_1 sin\theta_4 \\ n_1 sin\theta_1 = n_2 sin\theta_2 \end{cases}. \tag{9}$$

Substituting into Equation (8):

$$\begin{aligned} \mathrm{D} &= 2d\mathrm{n}_1\left(\frac{1}{\cos\theta_4} - \frac{sin^2\theta_4}{cos\theta_4}\right), \\ &= 2d\mathrm{n}_1 cos\theta_4 + \frac{\lambda}{2}, \\ &= 2d\sqrt{{n_1}^2 - {n_2}^2 sin^2\theta_3}, \\ &= 2d\sqrt{{n_1}^2 - {n_2}^2 sin^2\left(\frac{\pi}{4} - \theta_2\right)}, \\ &= d\sqrt{4{n_1}^2 - 2{n_2}^2 + 4n_1 n_2 sin\theta_1\sqrt{1 - \frac{{n_1}^2}{{n_2}^2}sin^2\theta_1}} \end{aligned} \quad (10)$$

If half-wave rectification was considered, then

$$\mathrm{D} = \frac{\lambda}{2} + d\sqrt{4{n_1}^2 - 2{n_2}^2 + 4n_1 n_2 sin\theta_1\sqrt{1 - \frac{{n_1}^2}{{n_2}^2}sin^2\theta_1}}. \quad (11)$$

Therefore, the interferogram, represented by D, was dependent on the distance d, the refractive indexes n_1 and n_2, and the incidence angle θ_1. The accurate measurement of $n_1, n_1,$ and θ_1 was difficult. In this project, therefore, a calibration process was conducted to model the relationship between D and d. When a constant C was defined as:

$$C = \sqrt{4{n_1}^2 - 2{n_2}^2 + 4n_1 n_2 sin\theta_1\sqrt{1 - \frac{{n_1}^2}{{n_2}^2}sin^2\theta_1}} \quad (12)$$

Equation (11) could be modified as:

$$\mathrm{D} = \frac{\lambda}{2} + C \cdot d. \quad (13)$$

During the movement, the phase shift of the interferogram was correlated with the changing of D, instead of the absolute value. Thus, Equation (13) could be modified as:

$$\Delta D = C \cdot \Delta d. \quad (14)$$

This linear relationship could be determined by observing the phase shift of the interferogram and measuring the distance h with a reference sensor:

As shown in Figure 5, a small angle was intentionally set between the optical flat and the moving axis of the stage. During the axial movement of the stage, the distance between the two optical surfaces gradually changed. The distance was measured by both the confocal sensor and the film interferometer. The images of the interferogram were captured continuously and the phase value of the central point was computed based on image processing, as shown in Figure 6.

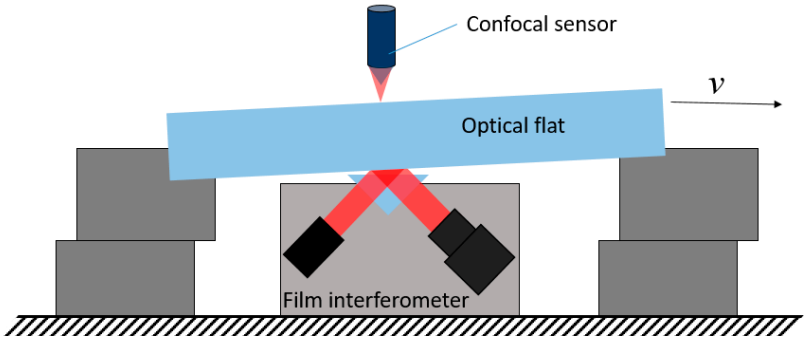

Figure 5. Calibration setup of the film interferometer.

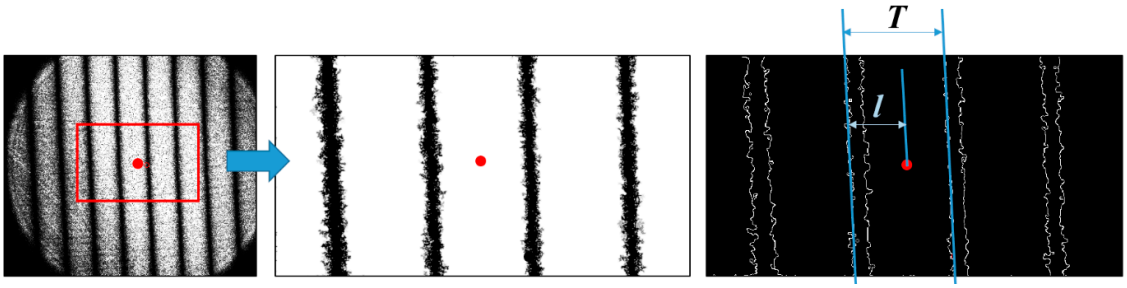

Figure 6. Image processing for phase calculation.

The interfergram did not show an ideal sinusoidal wave cycle due to high-order harmonics. Therefore, the edge detection technique was applied to identify the signal cycle. The position of the central point indicated its phase shift ω:

$$\omega = \left(m + \frac{l}{T}\right) \cdot 2\pi, \tag{15}$$

where m is the number of wave cycle shifts.

Although the angular motion errors may have changed the density and orientation of the interference stripes, the calculation of the phase using Equation (16) was not affected. The phase shifts calculated with Equation (16) and the distance change measured by the confocal sensor were plotted in the characteristic curve, as shown in Figure 7.

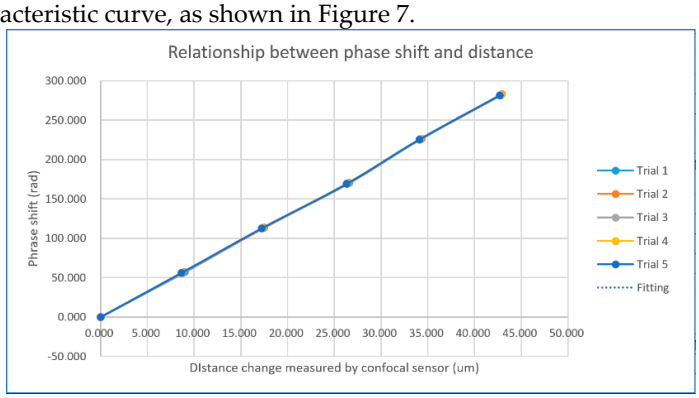

(**a**) Actual calibration results of the film interferometer

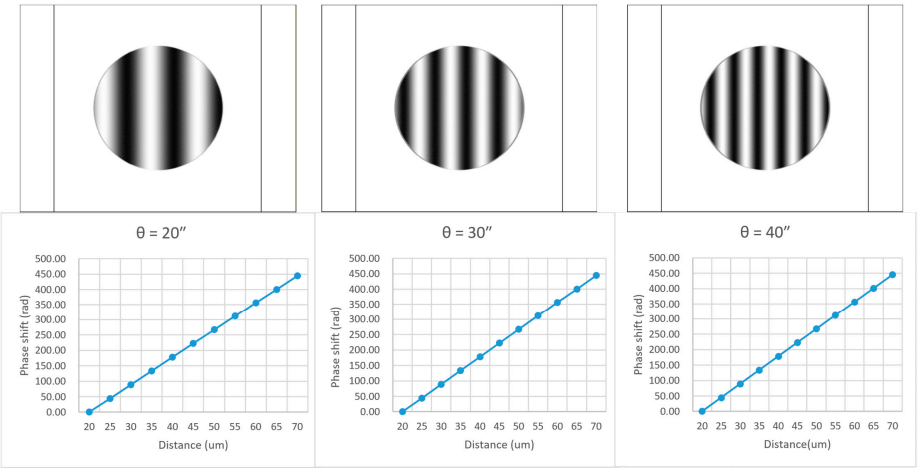

(**b**) Simulation results with different angles set between the reflective surfaces

Figure 7. Relationship between phase shift and distance.

In order to generate the fringe-type interferogram, the two reflective surfaces could not be exactly parallel with each other. A small angle was set to form an air wedge. During the movement, this angle might change due to the imperfect straightness of the guideway. In order to verify the model consistency when the angle changed, a simulation-based on Zemax was conducted. Different angles, 20″, 30″ and 40″ were set. As shown in Figure 7b, despite the different fringe densities, the relationship between distance and phase shift remained consistent. Therefore, the angle between the two reflective surfaces won't significantly affect the distance measurement at the central point.

It worth highlighting that the proposed film interferometer showed better stability compared with conventional Michelson interferometry designs. As shown in Figure 4, the interference occurred in the thin gap between the two optical surfaces, which was considered a relatively enclosed space. This optical structure, therefore, showed better robustness against temperature change and airflow.

4. Analysis of the Degree of Freedom

In order to allow a long travel range and to accommodate a differential measurement setup, the proposed system needed separate supporting and guiding mechanisms, as discussed in Section 2. Furthermore, the Abbe error-free design may have also introduced a separate guiding mechanism [31,33,34]. To avoid an over-constrained mechanism, a strict alignment and adjustment process was needed. The straightness and parallelism of the linear guides are very critical to such systems. In order to address this challenge, the proposed modular system was developed based on DoF analysis:

As shown in Figure 8, the key points of designing and assembling the system were those listed below:

1) There were one actuating module and two supporting modules in this system. Each supporting module consisted of two perpendicularly placed sliders, which were pre-assembled. This 2D sliding pair could be considered a plane contacting pair that allowed free movement in a horizontal plane despite possible in-plane placement errors.
2) The sliders were well leveled to the horizontal reference, assisted by an LVDT (Linear Variable Differential Transformer)
3) The stage top was rigidly connected with the actuating module, and it was coupled with the two supporting modules through ball hinges.

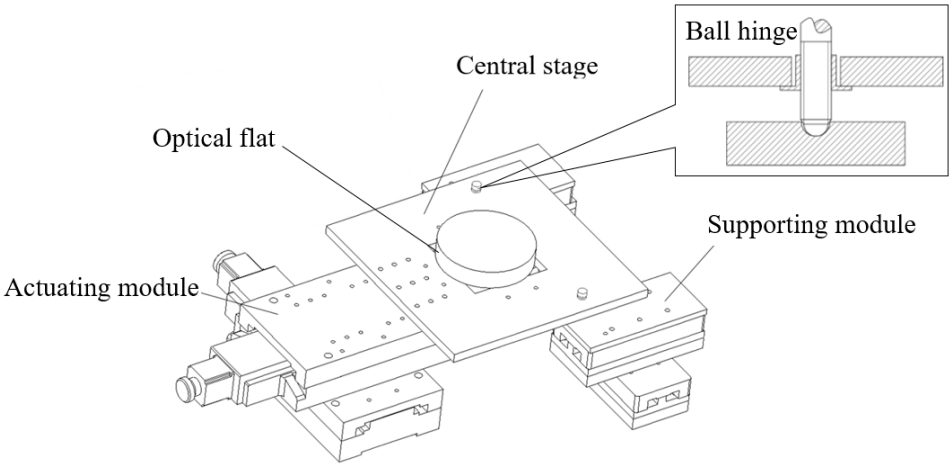

Figure 8. XY motion system.

The following paragraphs provide the DoF analysis of the mechanism.

Traditional DoF theory does not cover the scenarios of imperfect straightness or parallelism, and parallel linear guides are often considered redundant constraints [35]. This methodology, however, does not apply to precision positioning systems. Based on the traditional theory, the structure shown in Figure 8 could be simplified to the mechanism shown in Figure 9a. When imperfect straightness and parallelism were considered, the linear guides had to be represented by two-point contacting pairs instead of sliding pairs, as shown in Figure 9b. The DoF of the mechanism shown in Figure 9b could be expressed by:

$$\mathrm{DoF} = 3 \cdot \mathrm{n} - 2 \cdot \mathrm{p} - 1 \cdot \mathrm{q}. \quad (16)$$

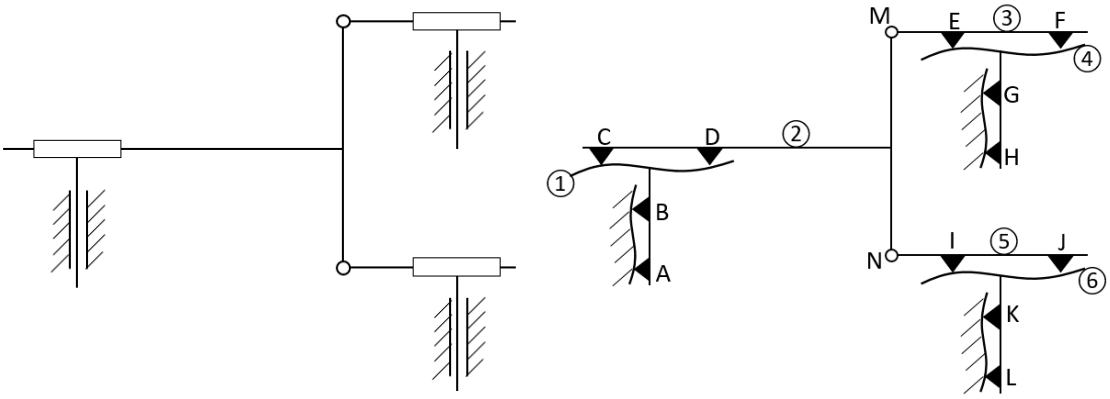

(**a**) Theoretical model: ideal components and ideal assembly

(**b**) Actual model: imperfect straightness parallelism

Figure 9. Mechanical model for DoF analysis: (**a**) Theoretical model: ideal components and ideal assembly, (**b**) Actual model: imperfect straightness parallelism.

In Equation (16), n is the number of components: n=6. p is the number of revolving pairs (ball hinges M and N), each of which was constrained to 2 DoF: p=2. q is the number of contacting pairs A to L, each of which was constrained to 1 DoF: q=12. The DoF of this mechanism could then be calculated to be two, which met the requirement of 2D motion.

Therefore, it was concluded that when the sliders were all well leveled and the 3D model could be projected to a 2D plane, an over-constrained mechanism would not be a concern for the proposed system. When a bigger measurement range is demanded in the future, this system can be easily reconfigured by replacing the actuating and supporting module with longer travel ranges.

With the assistance of an LVDT, the error of leveling could be controlled within a micrometer level, which would not affect the motion smoothness. The motion error due to the imperfect leveling can be detected by the film interferometer and compensated accordingly.

When a bigger measurement range is demanded, the system may need more supporting modules. As shown in Figure 9, one more supporting module would introduce two more components, one more revolving pair, and four more contacting pairs. By using Equation (16), it could be calculated that the additional DoF introduced by one more supporting module was zero, which meant more additional supporting modules would not affect the system DoF. With this modular design, therefore, the system had good scalability.

5. Experimental verification

In order to verify the system performance, experimental tests were conducted. This section provides the details for the experimental methodology and data analysis.

5.1.D topography measurement

A coin was scanned using the proposed system, with a scan range of 2 mm x 2 mm and a spacing of 10 μm. The experimental setup and the scanned image are shown in Figure 10.

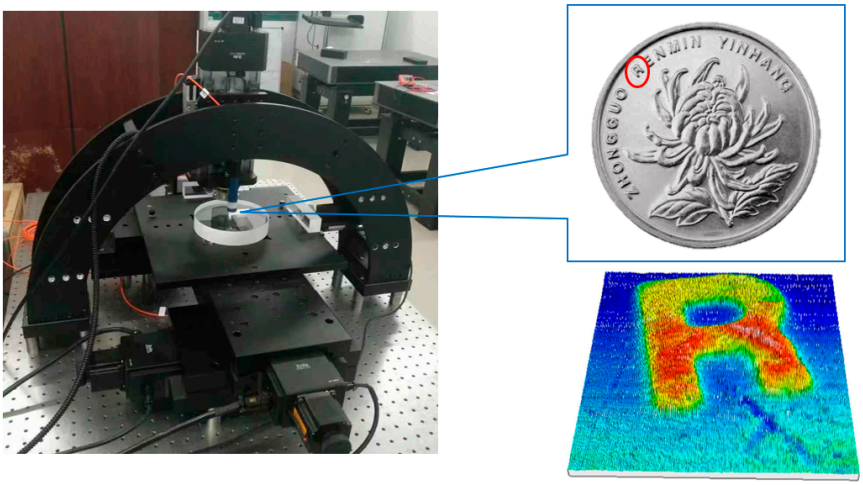

Figure 10. Experimental setup and coin scanning results.

In order to quantitatively evaluate the topography measurement performance, a set of roughness comparators was measured. Table 2 shows the comparison of the roughness parameters measured by the proposed system, namely, the HQU and a reference system, Mahr XR20. Each measurement was repeated five times. The average values are listed in Table 2. The standard deviation of each measurement was within 0.005 μm.

Table 2. Roughness measurement results.

Sample	Ra (μm)		Deviation (μm)	Deviation (%)	Rq (μm)		Deviation (μm)	Deviation (%)
	HQU	Mahr XR20			HQU	Mahr XR20	0.021	2.9%
1	0.589	0.602	0.602	2.2%	0.735	0.714	0.009	0.5%
2	1.493	1.471	1.471	1.5%	1.746	1.737	0.004	0.1%
3	2.736	2.728	2.728	0.2%	3.238	3.234	0.025	0.4%
4	5.842	5.810	5.810	0.6%	6.753	6.728		

It was shown that the proposed system was able to achieve nanometer accuracy when measuring surface roughness.

5.2. Step height measurement in a large area

The step height made by gauge blocks was measured at four different locations in the system measurement area of 100 mm × 100 mm. The scan length of each measurement was 50 mm. At each location, the measurements were repeated five times. Figure 11a shows the experimental setup and Figure 11b shows the profile measured by the differential sensors. The differential setup is discussed in Section 2. Sensor 1 (confocal sensor) was used to measure the heights from the top, while sensor 2 (film interferometer) was used to measure the straightness error from the bottom.

It was shown that the straightness error of the linear guide was effectively compensated for.

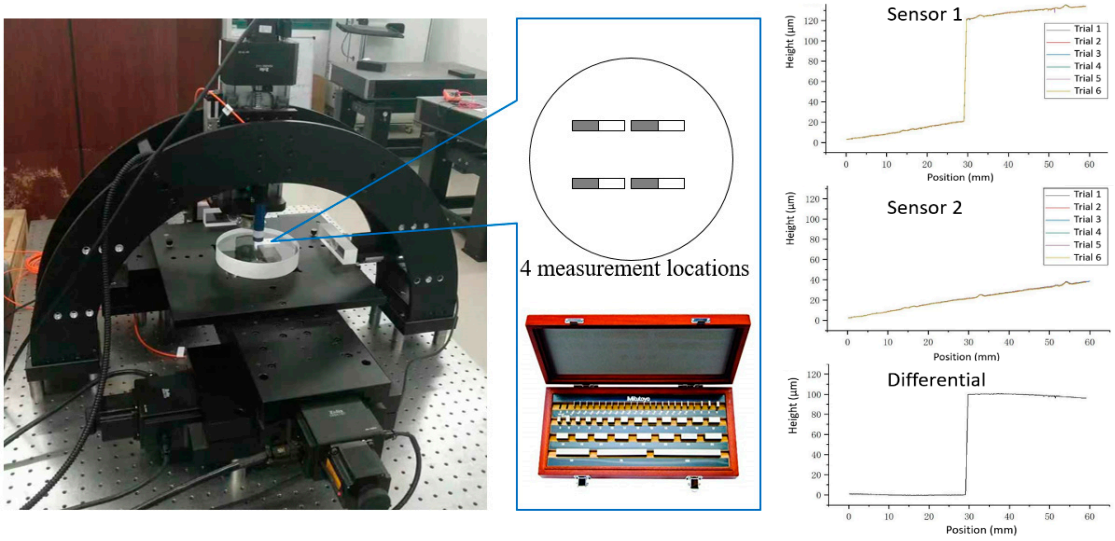

(**a**) Step height measurement setup (**b**) Measured profile

Figure 11. Step height measurement: (**a**) Step height measurement setup, (**b**) Measured profile.

Table 3 shows the measurement results.

Table 3. Step height measurement results.

	Location 1	Location 2	Location 3	Location 4
Step height measured (μm) (Nominal: 100.080 μm)	100.1910	100.1073	99.9984	99.9834
	100.1284	100.2008	99.9857	99.9637
	100.1179	100.1414	99.9284	99.9806
	100.2042	100.1783	100.0852	100.0523
	100.2156	100.1290	99.985	100.0361
Average (μm)	100.1715	100.1514	99.9965	100.0032
Repeatability σ (μm)	0.0451	0.0378	0.05648	0.03859
Reproducibility σ′ (μm)	0.09293			

The standard deviations of the repeated measurements at the same location and different locations were calculated, in order to represent the system's repeatability and reproducibility. The data in Table 3 shows that the repeatability and the reproducibility were within 100 nm.

6. Conclusion and discussion

In this paper, a concept of modular design for a high-accuracy measurement system is proposed. In the presented system, all of the components were standard components and easily available in the market. Instead of customizing high-accuracy built-in references, optical flats were applied in the proposed system to separate the geometric error caused by the mechanical components. The DoF analysis showed that this system could be easily assembled without special adjustment process. This system could also be easily scaled up for a bigger measurement range by introducing sliders with longer travel lengths.

The experimental results showed that the developed system was able to achieve nanometer repeatability and reproducibility for a surface topography measurement in the range of 100 mm × 100 mm.

The motivation for developing this system was to explore a generic methodology of setting up systems for high-accuracy topography measurements in a large area. Table 4 is the comparison between the presented system and other topography measurement technologies.

Table 4. Technology comparison.

Technologies	Measurement Resolution	Measurement area	Probe	Motion error compensation
Confocal microscopy	~10 nm	~1 mm	Optical	No
coherence scanning interferometry	~1 nm	~1 mm	Optical	No
Focus variation	~20 nm	~1 mm	Optical	No
Stylus profilometry	~1 nm	~100 mm	Contact	No
HQU developed system	~10 nm	100 mm	Optical	Yes
STM with high-precision stage [19]	Sub-nanometer	~1 mm	STM	Not stated
AFM with high-precision stage [20]	Sub-nanometer	~1 mm	AFM	Yes

As shown in Table 4, the optical topography measurement technologies, such as confocal microscopy, coherence scanning interferometry and focus variation are able to achieve nanometer vertical resolution in a millimeter measurement area. The measurement resolution and area are determined by the optical DOV (depth of view) and FOV (field of view) respectively. Stylus profilometry is able to perform the high-resolution measurements in a larger area but the contact probing mechanism limited its applications if the target surfaces are soft or have cleanliness requirements.

Compared with the measurement systems based on scanning tunneling microscopy (STM) or atomic force microscopy (AFM) [19,20], The proposed system is not an ideal solution for ultra-precision applications. The objective of this study was to develop a measurement system with sub-micron level accuracy in a measurement area up to 100 mm × 100 mm. Targeted applications of the proposed system include the metrological tasks in advanced manufacturing industries, such as semiconductor, consumer electronics, aerospace, etc.

This system is now working as a research platform for the authors' team. The authors' team has published some relevant work, including a confocal measurement system with expanded vertical measurement range [36], fast chromatic confocal sensor development [37], and image grating development for displacement measurement as an alternative of linear encoders [38]. These in-house developed technologies will be integrated into the prototype presented in this paper.

Author Contributions: Conceptualization, Fang Cheng; Methodology, Fang Cheng; Software, Jingwu Zou and Hang Su; Validation, Fang Cheng, Yin Wang and Qing Yu; Formal Analysis, Fang Cheng, Jingwu Zou and Hang Su; Investigation, Jingwu Zou and Hang Su; Resources, Qing Yu and Yin Wang; Data Curation, Jingwu Zou.; Writing-Original Draft Preparation, Fang Cheng.; Writing-Review & Editing, Fang Cheng.; Visualization, Jingwu, Zou.; Supervision, Fang Cheng; Project Administration, Yin Wang and Qing Yu.; Funding Acquisition, Qing Yu. All authors have read and agreed to the published version of the manuscript.

Funding: This research was funded by the National Natural Science Foundation of China (Grant No. 51505162) and the Science and Technology Program of Fujian, China (Grant No. 2019I0013).

Conflicts of Interest: The authors declare no conflict of interest.

References

1. Davim, J.P. *Surface Integrity in Machining*; Davim, J.P., Ed.; Springer: London, UK, 2010; ISBN 9781848828735.
2. Whitehouse, D. *Surfaces and Their Measurement*; Butterworth-Heinemann: London, UK, 2004; ISBN 978-1-903996-01-0.
3. Tay, C.; Wang, S.; Quan, C.; Shang, H. In situ surface roughness measurement using a laser scattering method. *Opt. Commun.* **2003**, *218*, 1–10.
4. Bain, L.E.; Collazo, R.; Hsu, S.; Latham, N.P.; Manfra, M.J.; Ivanisevic, A. Surface topography and chemistry shape cellular behavior on wide band-gap semiconductors. *Acta Biomater.* **2014,** *10*, 2455–2462.
5. Müller, T.; Kumpe, R.; Gerber, H.A.; Schmolke, R.; Passek, F.; Wagner, P. Techniques for analysing nanotopography on polished silicon wafers. *Microelectron. Eng.* **2001,** *56*, 123–127.
6. Lior, K. The influence of surface topography on the electromechanical characteristics of parallel-plate MEMS capacitors. *J. Micromech. Microeng.* **2005,** *15*, 1068.

7. Townsend, A.; Senin, N.; Blunt, L.; Leach, R.K.; Taylor, J.S. Surface texture metrology for metal additive manufacturing: A review. *Precis. Eng.* **2016,** *46*, 34–47.
8. Mediratta, R.; Ahluwalia, K.; Yeo, S.H. State-of-the-art on vibratory finishing in the aviation industry: An industrial and academic perspective. *Int. J. Adv. Manuf. Technol.* **2016,** *85*, 415–429.
9. Yoshizawa, T. (Ed.) *Handbook of Optical Metrology: Principles and Applications*; CRC Press: Boca Raton, FL, USA, 2009; ISBN 978-0-8493-3760-4.
10. Vorburger, T.V.; Rhee, H.G.; Renegar, T.B.; Song, J.F.; Zheng, A. Comparison of optical and stylus methods for measurement of surface texture. *Int. J. Adv. Manuf. Technol.* **2007**, *33*, 110–118.
11. Sandoz, P.; Tribillon, G.; Gharbi, T.; Devillers, R. Roughness measurement by confocal microscopy for brightness characterization and surface waviness visibility evaluation. *Wear* **1996**, *201*, 186–192.
12. Paddock, S.W. *Confocal Microscopy*; Humana Press: Totowa, NJ, USA, 1998; Volume 122, ISBN 1-59259-722-X.
13. Viotti, M.R.; Albertazzi, A.; Fantin, A.V.; Pont, A.D. Comparison between a white-light interferometer and a tactile formtester for the measurement of long inner cylindrical surfaces. *Opt. Lasers Eng.* **2008**, *46*, 396–403.
14. Danzl, R.; Helmli, F.; Scherer, S. Focus variation—A robust technology for high resolution optical 3D surface metrology. *J. Mech. Eng.* **2011**, *57*, 245–256.
15. Ebtsam, A.; Mohammed, E.; Hazem, E. Image Stitching based on Feature Extraction Techniques: A Survey. *Int. J. Comput. Appl.* **2014,** *99*, 1–8.
16. Henzold, G. *Geometrical Dimensioning and Tolerancing for Design, Manufacturing and Inspection,* 2nd ed.; Elsevier: Oxford, UK, 2006; ISBN 978-0750667388.
17. Xue, Y.; Cheng, T.; Xu, X.; Gao, Z. High-accuracy and real-time 3D positioning, tracking system for medical imaging applications based on 3D digital image correlation. *Opt. Lasers Eng.* **2017,** *88*, 82–90.
18. Bradley, C. Automated Surface Roughness Measurement. *Int. J. Adv. Manuf. Technol.* **2000**, *16*, 668–674.
19. Sawano, H.; Gokan, T.; Yoshioka, H.; Shinno, H. A newly developed STM-based coordinate measuring machine. *Precis. Eng.* **2012,** *36*, 538–545.
20. Wang, S.H.; Tan, S.L.; Xu, G.; Koyama, K. Measurement of deep groove structures using a self-fabricated long tip in a large range metrological atomic force microscope. *Meas. Sci. Technol.* **2011,** *22*, 094013.
21. Yang, P.; Takamura, T.; Takahashi, S.; Takamasu, K.; Sato, O.; Osawa, S.; Takatsuji, T. Development of high-precision micro-coordinate measuring machine: Multi-probe measurement system for measuring yaw and straightness motion error of *XY* linear stage. *Precis. Eng.* **2011,** *35*, 424–430.
22. Hsieh, T.; Chen, P.; Jywe, W.; Chen, G.; Wang, M. A Geometric Error Measurement System for Linear Guideway Assembly and Calibration. *Appl. Sci.* **2019,** *9*, 574.
23. Huang, Q.; Wu, K.; Wang, C.; Li, R.; Fan, K.C.; Fei, Y. Development of an Abbe Error Free Micro Coordinate Measuring Machine. *Appl. Sci.* **2016,** *6*, 97.
24. Bryan, J.B. The Abbe principle revisit: An updated interpretation. *Precis. Eng.* **1979**, *1*, 129–132.
25. Okuyama, E.; Akata, H.; Ishikawa, H. Multi-probe method for straightness profile measurement based on least uncertainty propagation (1st report): Two-point method considering cross-axis translational motion and sensor's random error. *Precis. Eng.* **2010,** *34*, 49–54.
26. Chen, X.; Sun, C.; Fu, L.; Liu, C. A novel reconstruction method for on-machine measurement of parallel profiles with a four-probe scanning system. *Precis. Eng.* **2019,** *59*, 224–233.
27. Jin, T.; Ji, H.; Hou, W.; Le, Y.; Shen, L. Measurement of straightness without Abbe error using an enhanced differential plane mirror interferometer. *Appl. Opt.* **2017,** *56*, 607–610.
28. Feng, W.L.; Yao, X.D.; Azamat, A.; Yang, J.G. Straightness error compensation for large CNC gantry type milling centers based on B-spline curves modeling. *Int. J. Mach. Tools Manuf.* **2015,** *88*, 165–174.
29. Chen, B.; Xu, B.; Yan, L.; Zhang, E.; Liu, Y. Laser straightness interferometer system with rotational error compensation and simultaneous measurement of six degrees of freedom error parameters. *Opt. Express* **2015,** *23*, 9052–9073.
30. Jäger, G.; Hausotte, T.; Manske, E.; Büchner, H.J.; Mastylo, R.; Dorozhovets, N.; Hofmann, N. Nanomeasuring and nanopositioning engineering. *Measurement* **2010**, *43*, 1099–1105.
31. Fan, K.-C.; Cheng, F. "The System and Mechatronics of a Pagoda Type Micro-CMM", Special Issue on Precision Micro- and Nano-Metrology for Nanomanufacturing. *Int. J. Nanomanufacturing* **2011,** *8*, 107–112.
32. Wirotrattanaphaphisan, K.; Buajarern, J.; Butdee, S. Uncertainty evaluation for absolute flatness measurement on horizontally aligned fizeau interferometer. *J. Phys. Conf. Series* **2019,** *1183*, 012009.

33. Vermeulen, M.; Rosielle, P.C.J.N.; Schellekens, P.H.J. Design of a high-precision 3D-coordinate measuring achine. *CIRP Ann. Manuf. Technol.* **1998**, 47, 447–50.
34. Fan, K.C.; Fei, Y.T.; Yu, X.F.; Chen, Y.J.; Wang,W.L.; Chen, F.; Liu, Y.S. Development of a low-cost micro-CMM for 3D micro/nano measurements. *Meas. Sci. Tech.* **2006**, *17*, 524–532.
35. Uicker, J.J.; Pennock, G.R.; Shigley, J.E. *Theory of Machines and Mechanisms*; Oxford University Press: New York, NY, USA, 2003.
36. Fu, S.; Cheng, F. Tegoeh, T. A Non-Contact Measuring System for In-Situ Surface Characterization Based on Laser Confocal Microscopy. *Sensors* **2018**, *18*, 2657.
37. Yu, Q.; Zhang, K.; Cui, C.; Zhou, R.; Cheng, F. Calibration of a Chromatic Confocal Microscope for Measuring a Colored Specimen. *IEEE Photonics J.* **2018**, *10*, 6901109.
38. Fu, S.; Cheng, F.; Tegoeh, T.; Liu, M. Development of an Image Grating Sensor for Position Measurement. *Sensors* **2019**, *19*, 4986.